Understanding airflow for enhancing Sepair performance

Nikki Hughes[1], *Marco* le Roux[1,*], *Quentin P.* Campbell[1], and *Abraham F.* van der Merwe[1]

[1]School of Chemical and Minerals Engineering, North-West University, South Africa

Abstract. In this study, a laboratory-scale negative pressure fluidization air gravity separation unit was employed to conduct air velocity tests. Subsequently, computational fluid dynamics (CFD) modelling was utilized to gain insights into the airflow profile and associated properties. The investigation examined three distinct airflow intensities corresponding to low, medium, and high suction fan settings of 10, 30, and 50 Hz. These airflow measurements were conducted across four sections of the suction nozzle: the fan-side (FS) inlet, other-side (OS) inlet, connecting pipe, and fluidizing box. The comparison between the modelled and experimental velocities reveals a significant level of agreement, as evidenced by high coefficients of determination (R2) which provide an indication of the extent to which the experimental variable explains the variation in the response variable. However, some deviations were observed in the predicted variables, as indicated by the root mean square error (RMSE), which indicates the predictive capability of the regression model in estimating the value of the response variable. The RMSE must be observed in the context of the actual airflows, which it represents in that if the RMSE is significantly lower than the observed airflow, the predictive capability of the regression model is considered accurate. Specifically, for the low flow system of 10 Hz, the R2 and RMSE values were determined as 0.95 and 1.13 m/s respectively. Similarly, for the medium flow system of 30 Hz, the R2 and RMSE values were found to be 0.93 and 4.09, respectively. Lastly, for the high-flow system, the R2 and RMSE values were obtained as 0.94 and 6.78, respectively. The comparison of the RMSE to the average observed velocity in the inlets and connecting separating units indicates that the predictive capability of the model is good, with minimal deviation in the predicted and observed variables. The similarity between the RMSE and the velocity in the fluidizing box shows a lower accuracy of the predicted values in this section.

1 Introduction

Air-based gravity separators have garnered considerable attention within the context of coal beneficiation due to the urgent challenges posed by water scarcity, pollution [1], dwindling coal reserves, remote and small-scale mining operations [2], as well as the processing of fine

* Corresponding author: marco.leroux@nwu.ac.za

materials [3]. Among the various processes available, one that is new and not fully understood yet is negative pressure fluidization processes.

Negative pressure fluidization employs a system design that harnesses the power of a suction fan to generate an adequately forceful airflow, thereby inducing fluidization and subsequent segregation of particles based on their size, density, and shape. Extensive exploration of different process designs is evident in the existing literature. For instance, Moszko et al. [4] investigated a process called 'AMSEP' for coal processing of mine-originating wastes. Stepanenko [5] examined and commercialized the Sepair system for processing various ores based on particle size, shape, and density, while Stanczyk et al. [6,7] explored the negative pressure pneumatic separator (NPPS) for hard coal beneficiation.

This study adopts a design akin to the Sepair [5] and seeks to comprehend the airflow characteristics by conducting experiments and utilizing computational fluid dynamics (CFD) modelling to establish a velocity profile. Gaining understanding of the airflow within the separation unit can provide valuable insights for assessing the suitability and applicability of the SEP-AIR for coal beneficiation. Furthermore, this information can guide the optimization of the process for specific applications, ensuring its effectiveness and efficiency.

1.1 Importance of airflow characteristics

In a system where air functions as the fluidizing medium, a comprehensive understanding of airflow behaviour and patterns assumes paramount importance in evaluating the suitability and applicability of the process. The characteristics of airflow directly impact the fluidization properties, thereby influencing the movement of particles [8]. Obtaining insights into these characteristics can facilitate optimized system design, determination of process scale, and establishment of operating parameters that ensure appropriate air flow, speed, and distribution. As a result, proper movement and stratification of particles are ensured, leading to enhanced separation efficiency, recovery rates, reduced energy consumption, and safe operation [9]. Moreover, comprehension of airflow characteristics enables troubleshooting and identification of root causes behind inefficient or uneven separation, particle misplacement, and blockages, which may contribute to operational issues.

2 Description of the lab-scale separation unit and function

To examine the properties, behaviour, and patterns of airflow, a laboratory-scale separating unit was meticulously designed, constructed, commissioned, and subsequently optimized, following the manufacturer's specifications. This section presents a comprehensive description of the unit's geometry, placement, and a summary of the anticipated airflow patterns and particle movement within. The processing unit comprises the following sections:

- **Feed**, consisting of a manual conveyor system for particle entry.
- **Separating unit**, where the fluidization and separation of the particles occur.
- **Centrifugal fan**, providing the suction force required.

The separating unit is composed of four distinct compartments, namely: (1) fluidizing chamber, (2) vortex chamber, (3) connecting pipe, and (4) collection bin. Figure 1 illustrates a schematic representation of the compartments, numbered from 1 to 4 in sequential order.

Each compartment within the system is specifically designed to exhibit distinct airflow patterns, thereby serving a particular function. Due to the draft induced by the suction fan, air enters horizontally from the environment over the feed belt and into the fluidizing box.

Subsequently, it progresses into the vortex chamber, where the circular arrangement induces the formation of a vortex. As the cyclic airflow proceeds from the vortex chamber to the connecting pipe, which possesses a smaller circular cross-section, it accelerates in accordance with Bernoulli's principle. Upon entering the larger collection bin, the air decelerates once again and exits through the suction fan.

The combination of the vortex chamber and connecting pipe functions as a "particle capturing" mechanism, whereby the circulating air seizes fluidized particles at the nozzle height, accelerating them for collection in the product bin. Additionally, the vortex chamber contributes to the establishment of a uniform airflow profile spanning the length of the separating nozzle, mitigating the occurrence of dead spots in the region furthest from the suction fan. The positioning of the fluidizing box above the feeding conveyor also influences the properties of the air within the air inlets. Decreasing the gap size leads to an increase in air velocity, potentially affecting the velocity profile within the fluidizing box. Nevertheless, the particle size range predominantly determines the appropriate gap height, ensuring unobstructed particle flow into the inlet of the fluidizing box. As a general guideline, a gap height equivalent to 1.5 times the size of the largest particle in the feed is recommended. Figure 1 illustrates various perspectives of the laboratory-scale separating unit.

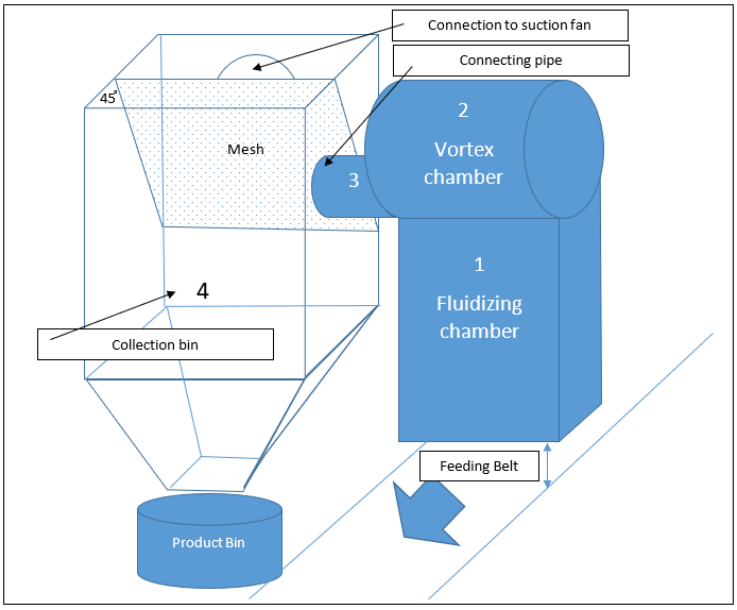

Fig 1: Separating compartments of the laboratory scale Sepair unit.

A straightforward particle feeding system is employed to introduce particles into the separation nozzle at a predetermined load and velocity. The suction force is generated by utilizing a Trojan BC60 series direct drive, 1.1 kW centrifugal fan capable of reaching 3000 RPM. Information regarding the unit's geometry is presented in Table 1.

Table 1: Dimensions of the laboratory scale separation unit

	Fluidizing chamber (mm)	Collection bin (mm)	Vortex chamber (mm)	Connecting pipe (mm)
Length	300	600	300	150
Width	100	600	-	-
Height	300	600	-	-
Diameter	-	-	160	80

3 Model development

The primary focus of this study revolves around the airflow patterns within the suction nozzle (compartments 1, 2, 3 and feeding belt in Figure 1). A three-dimensional assembly including the feed conveyor plate, air inlets, fluidizing box, vortex chamber, connecting pipe and air outlet was created utilizing Siemens NX-12. This geometry was used to define the boundaries for the simulation of air flow patterns in STAR-CCM+ and is visually depicted with compartments, inlets and outlet labelled in Figure 2.

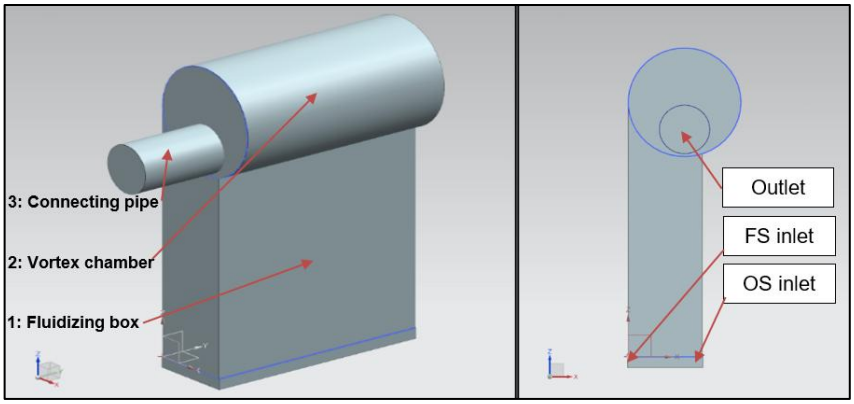

Fig 2: Suction nozzle assembly constructed in NX-12, trimetric view with compartment labelled (left) and front view with inlets and outlet labelled (right).

3.1 Meshing and boundary conditions

Various meshing strategies are available, each offering distinct advantages and applications. In this study, the assembly was exported as para-solid files from NX-12 and subsequently imported into STAR-CCM+ as a surface mesh. Parts within the assembly were assigned to specific regions, with each part surface assigned a corresponding boundary. The inlet and outlet regions, as illustrated in Figures 2 and 3, were designated with a specific type and boundary condition, namely velocity inlet and pressure outlet, respectively. The outer surface of the suction nozzle and bottom of the feeding belt were deemed walls.

For surface meshing, a surface remesher was employed. This remesher ensures the generation of a high-quality discretized mesh suitable for CFD simulations. It accomplishes this by re-triangulating the surface based on a specified edge length, while also allowing for the omission of selected surfaces while preserving the original features of the imported mesh. To generate the volume mesh, the polyhedral mesher option was chosen. This method

constructs a volume mesh composed of polyhedral-shaped cells. It has proven to be numerically stable and accurate compared to the tetrahedral mesh, while also resulting in a reduced number of cells. Additionally, the prism layer mesher, an optional feature, was employed. It adds prismatic cell layers adjacent to wall boundaries, aiding in the prediction of flow characteristics such as drag force and pressure drop. Furthermore, it refines the mesh around regions with sharp edges or small openings, where flow descriptions become more complex [10].

A base size of 5 mm was selected for the mesh cells yielding 144,129 cells, 867,278 cell faces and 703,627 cell vertices. Figure 3 illustrates the resulting mesh, as well as the inlet and outlet regions generated for the laboratory-scale separation nozzle using the aforementioned meshing strategy.

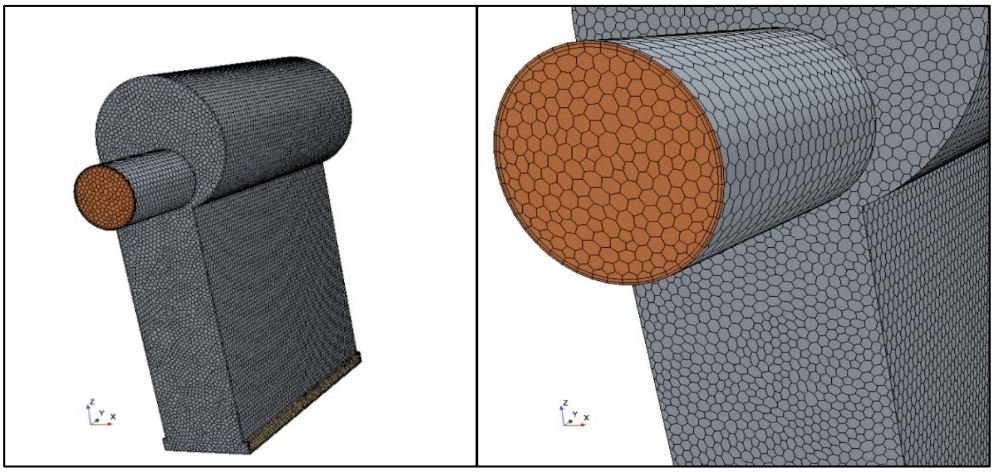

Fig 3: The mesh generated throughout the unit, full view (left) and zoomed view of the cells (right).

The inlet and outlet regions, depicted in orange, can be observed in Figure 3. The air inlet comprises the open sections on either side between the conveyor and nozzle, which were designated as velocity inlets. At these locations, the air enters the system with a defined velocity, traverses through the unit, and exits via the connecting pipe, which serves as the air outlet, assigned as a pressure outlet. In the magnified image on the right, the volume mesh is clearly visible, characterized by polyhedral-shaped cells. Additionally, adapted cells near the edges are evident, indicating a refined mesh configuration in these regions.

3.2 Governing equations

The governing equations used by STAR-CCM+ to solve fluid dynamics problems incorporate physics models that account for space, time, motion, material properties, and turbulence. These equations also include the three fundamental conservation laws: (1) continuity, (2) momentum, and (3) energy [11]. Within each of these categories, STAR-CCM+ offers numerous models, providing a vast array of choices and combinations. The selection of an appropriate combination of physics models is crucial to ensure that the simulation accurately captures the essential physics relevant to the specific problem being investigated. This entails considering factors such as turbulence, multiphase flow, heat transfer, and chemical reactions. Neglecting or misrepresenting important physical phenomena can result in unrealistic and unreliable outcomes, leading to misleading conclusions and inefficient utilization of computational resources [12,13].

In this study, turbulence was modelled using the Reynolds-Averaged Navier–Stokes (RANS) approach, which is widely adopted in CFD due to its balance between computational efficiency and predictive capability. The RANS model simplifies the Navier–Stokes equations by decomposing the instantaneous flow variables into mean and fluctuating components, allowing the simulation to focus on the time-averaged behaviour of turbulent flows. This introduces additional terms known as Reynolds stresses, which are modelled using turbulence closures such as the k-ε, k-ω, or SST (Shear Stress Transport) models.

For the current application involving airflow through a suction nozzle, the RANS model is particularly suitable due to its ability to handle complex internal flows with recirculation and boundary layer effects, while maintaining reasonable computational cost. Recent advancements in RANS-based transition modelling have demonstrated improved accuracy in predicting boundary-layer behaviour and flow separation, especially when coupled with adaptive mesh refinement techniques [14]. Moreover, RANS models have shown reliable performance in predicting engineering quantities such as pressure drop and velocity distribution in similar internal flow configurations [15].

Table 2 provides an overview of the chosen combination of physics models specifically selected for the current study.

Table 2: Flow diagram representing the physics model selection for STAR-CCM+ [11,13,16].

Space	Three dimensional
The three-dimensional spatial model is implemented on three-dimensional meshes, wherein all spatial directions hold significance	
Time	Steady State
The steady-state time model is utilized specifically when discretizing spatial derivatives. In accordance with the methodology outlined in literature, the steady-state time model is deemed appropriate for the current study.	
Material	Single component gas
The single-component material models are employed for the modelling of pure substances in their fundamental states, namely gas, liquid, and solid.	
Equation of state	Constant density
The constant density EOS can be used for single-phase flows, non-reactive flows and incompressible flows where Mach<1.	
Fundamental equation	Conservation
The conservation of mass, momentum ad energy equations are applied.	
Turbulence	Reynolds-Average-Navier-Stokes and Reynolds Stress Turbulence
The Reynolds stress turbulence model is widely acknowledged for highly swirling or strongly segregated flow.	
Optional	Optional models selected
• Gradients	

- Exact wall distance and Two-layer All y+ wall treatment

3.3 Solution algorithm and convergence

As stated previously, the outlet of the connecting pipe was configured as a pressure outlet, with boundary condition pressure values of -125 Pa, -1150 Pa, and -3000 Pa for the low, medium, and high flow systems respectively. These pressure values were acquired from the laboratory-scale unit through physical measurements of pressure in the connecting pipe using a Fluke 922 airflow and manometer. This information serves to provide the simulation with the magnitude of the suction force boundary condition observed at various flow intensities. Velocity values obtained through physical measurements were also included in the air inlets and pressure outlet as initial conditions to aid the numerical calculations and convergence.

Convergence in STAR-CCM+ is typically assessed using residual monitors and a specified velocity, force or pressure coefficient. The residuals represent the discrepancies between the solved discretized equations and their respective values are calculated by root-mean-square averaging [10]. By default, the residuals of the continuity equation, the X-, Y-, and Z-momentum equations, as well as the turbulent kinetic energy and turbulent dissipation rate, are continuously monitored and plotted. Overall convergence of the simulations was determined by ensuring that the residuals of the variables decrease to values below 1E-03 [13]. As for final convergence, pressure values in the connecting pipe were monitored. Convergence was deemed achieved when the pressure exhibited stability and varied by less than 0.1 Pa per iteration.

4 Experimental method

A series of physical airflow tests were carried out within distinct sections of the separating unit to examine the actual airflow behaviour and compare it with the model-generated results. The primary focus of these experiments was to assess airspeed and flow direction, as these factors play a critical role in determining the adequacy of suction force required to transport specific particles.

Air velocity measurements using a Testo smart probe anemometer were conducted at various positions within the unit, including 40 different locations. These measurements encompassed five locations spanning both inlets each, three locations spanning the connecting pipe, and nine locations covering the area of the fluidizing box at three different depths. The measurements were taken for ten suction fan settings, and ten readings were recorded for repeatability. Figure 4 provides schematic of the unit, indicating the points where air velocity tests were conducted.

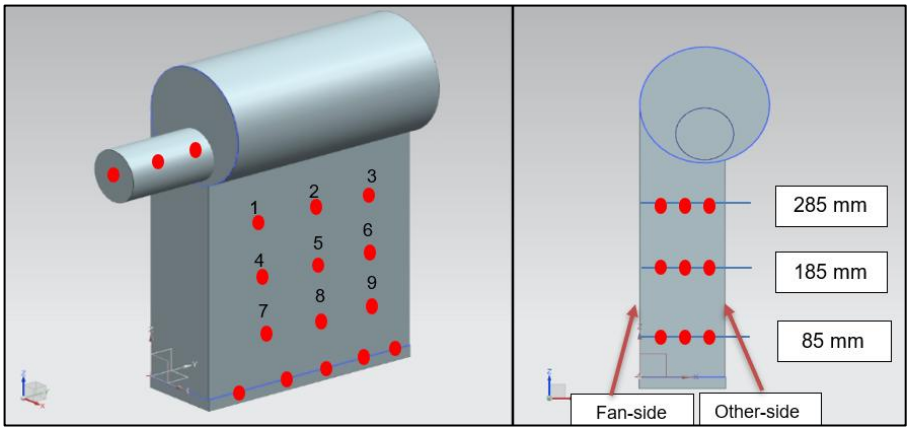

Fig 4: Access point for velocity measurements.

To assess the stability of the velocity profile, additional measurements were captured every second over a duration of one minute. This monitoring process aimed to ensure the consistency of the velocity distribution within the system. An s-type pitot tube, in conjunction with a Fluke anemometer, was employed to determine the direction of airflow. In this configuration, a negative airflow reading indicated a flow opposite to the predicted airflow direction. These measurements provided valuable insights into potential eddying currents and facilitated a comparison between the velocity vectors obtained from the simulation and the measured airflow direction. Furthermore, to validate the obtained airflow direction, smoke tests were conducted. Videos were recorded as smoke generated from a fog machine permeated through the suction unit under different suction fan settings. These visual observations served as a confirmation of the airflow direction determined through the analytical analysis and simulation.

5 Results

The velocities obtained from the experiments were carefully examined to assess their stability and repeatability. Subsequently, they were compared to the simulation results at three different flow intensities (low, medium, and high). This comparison was conducted using parity plots in conjunction with statistical measures such as the coefficient of determination (R^2) and root-mean-squared-error (RMSE).

5.1 Experimental airflow, direction and repeatability

Table 3 presents the mean magnitudes of velocity and associated Reynolds numbers observed in specific regions of the separation nozzle for each flow intensity considered. The flow direction is also depicted as an axis on the Cartesian plane (as illustrated in Figure 4). Moreover, standard deviation values are provided to assess the consistency and repeatability of the measured velocity values.

Table 3: The mean velocity and standard deviations for each fan setting.

	Mean velocity (m/s)	**Standard deviation**	**Direction cartesian plane**	**Reynolds number**	**Flow regime**
	Low flow system				
Fan-side inlet	4.13	±0.26	+X	16,305	Turbulent
Other-side inlet	3.82	±0.01	-X	15,081	Turbulent
Connecting pipe	14.34	±0.17	-Y	75,483	Turbulent
Fluidizing box					
8.5 cm (from inlet)	2.61	±1.01	±Z	34,346	Turbulent
	1.74	±0.63	±Z	22,898	Turbulent
18.5 cm (from inlet)	1.44	±0.62	±Z	18,950	Turbulent
28.5 cm (from inlet)					
	Medium flow system				
Fan-side inlet	12.80	±0.64	+X	50,533	Turbulent
Other-side inlet	11.94	±0.70	-X	47,138	Turbulent
Connecting pipe	46.86	±0.76	-Y	257,190	Turbulent
Fluidizing box					
8.5 cm (from inlet)	8.69	±3.07	±Z	114,357	Turbulent
	4.75	±1.28	±Z	62,508	Turbulent
18.5 cm (from inlet)	4.54	±1.39	±Z	59,744	Turbulent
28.5 cm (from inlet)					
	High flow system				
Fan-side inlet	21.27	±0.92	+X	83,971	Turbulent
Other-side inlet	20.54	±0.84	-X	81,089	Turbulent
Connecting pipe	75.52	±1.20	-Y	397,524	Turbulent
Fluidizing box					
8.5 cm (from inlet)	14.91	±5.06	±Z	196,209	Turbulent
	8.39	±1.73	±Z	110,409	Turbulent
18.5 cm (from inlet)	8.54	±2.25	±Z	112,383	Turbulent
28.5 cm (from inlet)					

The low standard deviations observed in the inlets and connecting pipe indicate the repeatability and accuracy of the recorded velocity readings in these regions. However, larger standard deviations are noticeable in the velocity measurements within the fluidizing chamber. This variation can be attributed to the development of a more intricate velocity profile across the cross-section of the fluidizing chamber in the horizontal plane (z-direction). Mean velocity or standard deviation calculations alone over the horizontal plane do not adequately capture this complexity. Specifically, consistently higher velocities are observed

in the middle section (width wise) of the fluidizing chamber, while lower velocities are found closer to the walls. Experimental measurements obtained using the s-type pitot probe reveal a variable flow direction in the near-wall region, suggesting the presence of eddying currents that impede the airspeed. Moreover, the top horizontal plane exhibits higher velocities toward the side of the connecting pipe, indicating the influence of the vortex located just above. Notable is that the velocities obtained in the different sections of the suction nozzle all relate to Reynolds number exceeding 2,800 and thus the airflow within the unit can be considered turbulent. Figure 5 offers a horizontal cross-sectional view in the z-direction, specifically at distances of 8.5 cm, 18.5 cm, and 28.5 cm from the inlet within the fluidizing box (visible by the lines in the right image of Figure 4). This table presents the velocity data obtained from the 27 measurement points, providing valuable information regarding the observed velocity profile. In Figure 4, we can discern the locations of the 9 measurement points in the image on the on the left and the corresponding positions, categorized into three distinct depths and three elevations in the image on the right.

Low flow sytem

	x/y	1	2	3
Z plane 28,5 cm Top	3	0,80	1,54	1,18
	2	0,73	1,51	2,02
	1	0,98	1,03	1,52
		4	5	6
Z plane 18,5 cm Middle	3	0,96	2,25	0,91
	2	1,65	2,66	1,69
	1	1,69	1,36	1,68
		7	8	9
Z plane 8,5 cm Bottom	3	1,34	3,21	1,36
	2	4,27	2,79	3,85
	1	3,27	2,03	3,19

Medium flow system

	x/y	1	2	3
Z plane 28,5 cm Top	3	2,09	4,15	5,27
	2	4,31	5,41	7,38
	1	3,70	3,57	5,02
		4	5	6
Z Plane 18,5 cm Middle	3	2,51	5,55	2,70
	2	5,20	6,85	5,12
	1	4,83	4,92	5,03
		7	8	9
Z Plane 8,5 cm Bottom	3	4,99	9,57	5,07
	2	13,54	8,94	13,79
	1	8,66	6,39	7,23

High flow system

	x/y	1	2	3
Z plane 28,5 cm Top	3	7,06	8,61	10,27
	2	4,62	7,44	13,41
	1	8,30	8,61	8,54
		4	5	6
Z Plane 18,5 cm Middle	3	4,64	9,85	6,37
	2	9,53	10,37	9,29
	1	8,84	7,83	8,76
		7	8	9
Z Plane 8,5 cm Bottom	3	9,04	17,65	8,22
	2	22,91	16,30	22,40
	1	14,27	11,37	12,01

Fig 5: The velocity in the fluidizing chamber as horizontal planar views in the z-direction.

The coefficients of variation for velocity readings, measured at one-second intervals over a one-minute duration at specific locations within the fluidizing box, exhibit a range of 0.02–0.60, 0.10–0.79, and 0.21–0.79 for the low, medium, and high-flow systems, respectively. These values signify minimal variations in velocity readings over time, indicating a high level of stability in the measured velocities over time.

5.2 Comparison of observed and simulated data

To compare the simulated velocities with the experimental velocities, point vectors were employed in STAR CCM+ to ascertain the speed and direction of the airflow. These vectors were placed at the identical positions as the 40 measuring points within the suction nozzle in the experimental setup.

Parity plots, along with their associated coefficient of determination (R^2) and root-mean-squared-error (RMSE) were utilized to describe the correlation between the observed and simulated velocities. These statistical measures provide valuable insights into the agreement between the two sets of velocities. The R^2 value indicates the extent to which the experimental variable elucidates the variation in the response variable while the RMSE serves as an indicator of the predictive capability of the regression model in estimating the value of the response variable. A high R^2 value, accompanied by low RMSE value, indicates a strong correlation between the observed and predicted values. Nevertheless, it is essential to assess the RMSE in relation to the average magnitude of the observed values. By considering the context of the average observed values, a more comprehensive evaluation of the predictive accuracy can be achieved [17].

5.3 Simulated airflow results

Figure 6 displays parity plots illustrating the comparison between the simulated velocities and the experimental velocities for all three flow systems. The corresponding statistical values obtained from this analysis are as follows: for the low flow an R^2 value of 0.95 and RMSE value of 1.13, for the medium flow an R^2 and RMSE value of 0.93 and 4.09 respectively and for the high flow an R^2 value of 0.94 while the RMSE value is 6.78.

Based on Figure 6 and the corresponding statistics, it can be observed that there is generally good agreement between the modelled and observed velocity ranges for all the flow system. Most velocity magnitudes and directions exhibit alignment between the datasets, indicating a satisfactory level of agreement. However, notable disparities were observed, primarily within the fluidizing box, particularly in the near-wall regions, where both magnitude and direction of velocities show occasional deviations. This observation is supported by the RMSE values of the three flow regimes, which in all three cases are significantly lower than the average velocities measured at the inlets and in the connecting pipe. However, the RMSE in the fluidizing box resembles the mean velocity measured over the entire section. This deviation in the fluidizing box is ascribed to the influence of the vortex at the top, extending into this section and crating irregular eddies, especially near the walls of the vessel.

5.4 Visual representation of simulated results

Figures 7, 8 and 9 exhibit the results of the CFD simulations conducted on the low, medium, and high flow systems, respectively. These figures present cross-sectional illustrations of the suction nozzle, depicting vector streamlines in the side view (x-direction, A1) and front view (y-direction, B1), which effectively illustrate the speed and direction of the velocity. Additionally, scalar images of the same cross-sectional perspectives (A2 and B2) are included to emphasize regions with reduced flow.

To facilitate a comparison, velocity vectors and velocity scalars at each of the 40 points where physical airflow measurements were taken are depicted in the images labelled C1 and C2. These visual representations provide valuable insights into the flow patterns that develop within the suction nozzle, with particular attention given to flow speed and direction. These insights help identify potential dead spots and eddying currents within the system.

For the low flow system, represented in Figure 7, it is evident that the inlet flow initially progresses horizontally (visible in schematic A1 and C1) and then curves upward in the centre of the fluidizing box tending towards the fan-side (FS) (schematic A1). The development of a circular vortex flow can be observed in the vortex chamber (A1) and exits through the connecting pipe (B1). Variations in airspeed and changes in flow direction are apparent, indicating regions of fast (red) and slow (blue) airflow (figures A1, A2, B1 and B2) as well as areas where the flow direction alters (A1, B1 and C1). The arrows in C1 are vectors of the measuring points and indicated the direction of flow. Noteworthy is that these vectors are portrayed in relation to the velocity scalar to which they respond, hence a large difference in velocities will result in a large difference in arrow size. Additionally, the presence of potential dead spots becomes apparent as visible with darker blue regions in A2, B2 and C2. Moreover, eddying currents are noted by the vector arrows observed in A1. Consistent with the experimental findings, these eddying currents, low flow regions, and dead spots are predominantly observed near the walls of the unit. Similar views are provided for the medium and high flow systems in Figures 8 and 9, respectively.

An intriguing observation is that the model exhibits a distinct velocity profile for the low flow system, contrasting with the medium and high flow systems. The latter systems display a noticeable s-shape flow profile that is absent in the low flow system. In contrast, the experimental velocities for all three flow systems demonstrate the pronounced s-shape airflow pattern as visible in Figure 5. This profile contributes to the formation or intensification of eddying currents, regions with low flow, and dead spots near the walls. The development of unique profile can be attributed to the way the air is drawn through the vortex chamber and connecting pipe, as well as the design of the air inlets and the shape of the unit. Furthermore, similar regions with low flow are observed in the region below where the fan-side and other-side inlets meet in the middle of the fluidizing box and the vicinity where the vortex flow interacts with the upward airflow current (this is noted with the dark blue regions in image A2).

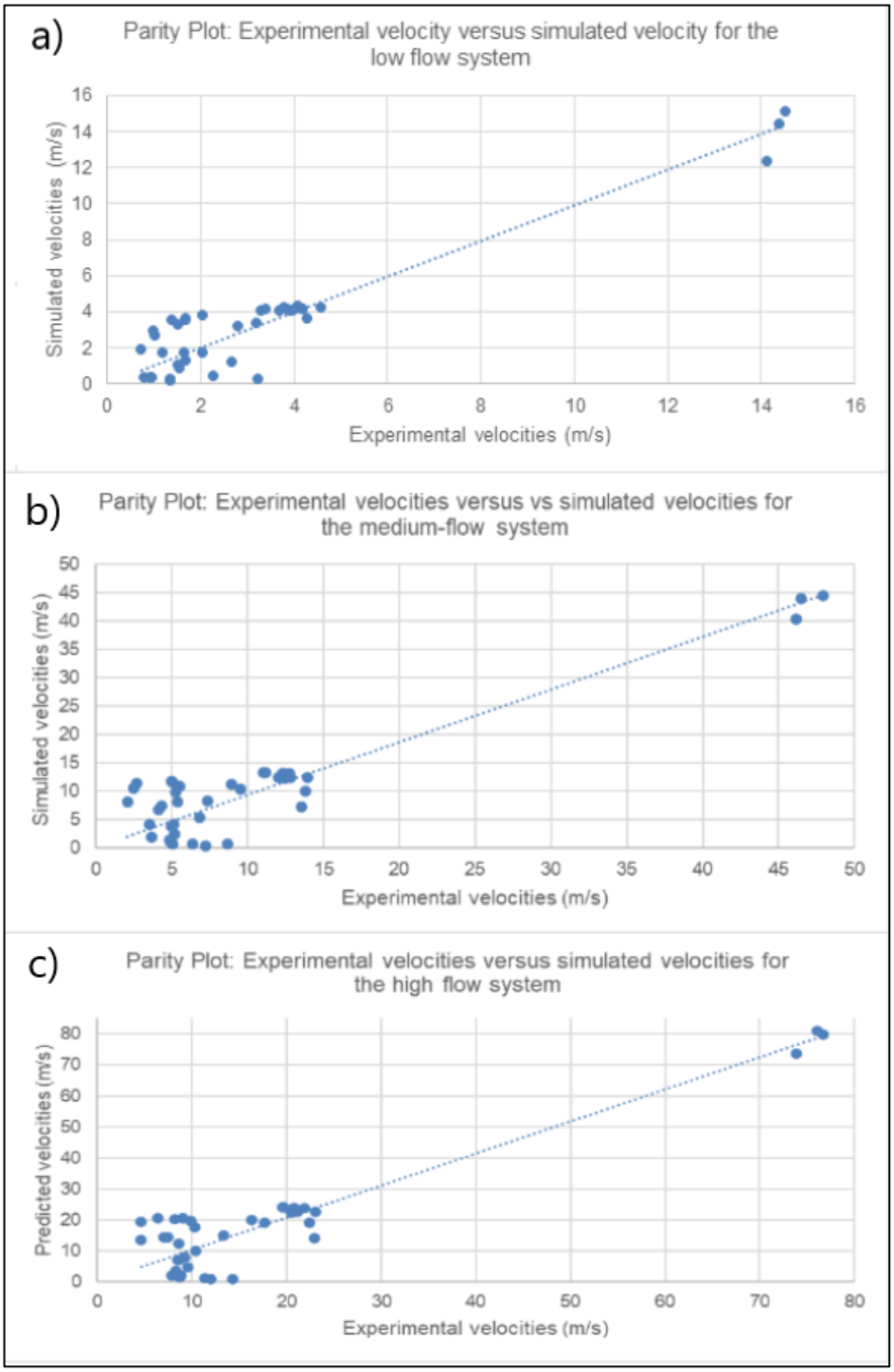

Fig 6: Parity plots for the a) low flow, b) medium flow and c) high flow system.

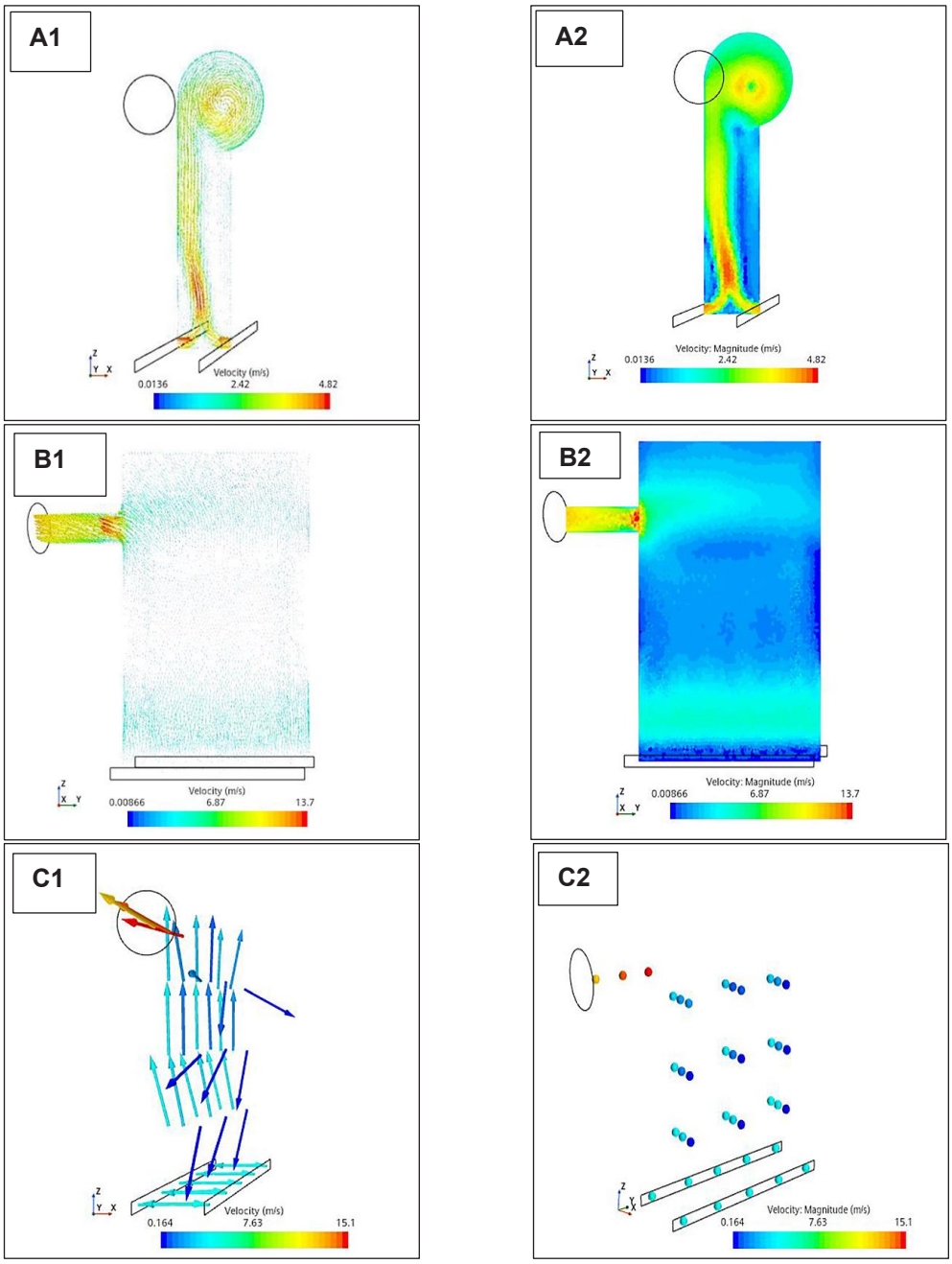

Fig 7: CFD simulation results portraying planar views of velocity vectors (A1, B1 and C1) and velocity scalars (A2, B2 and C2) of the airflow in the suction nozzle for the low flow system**.**

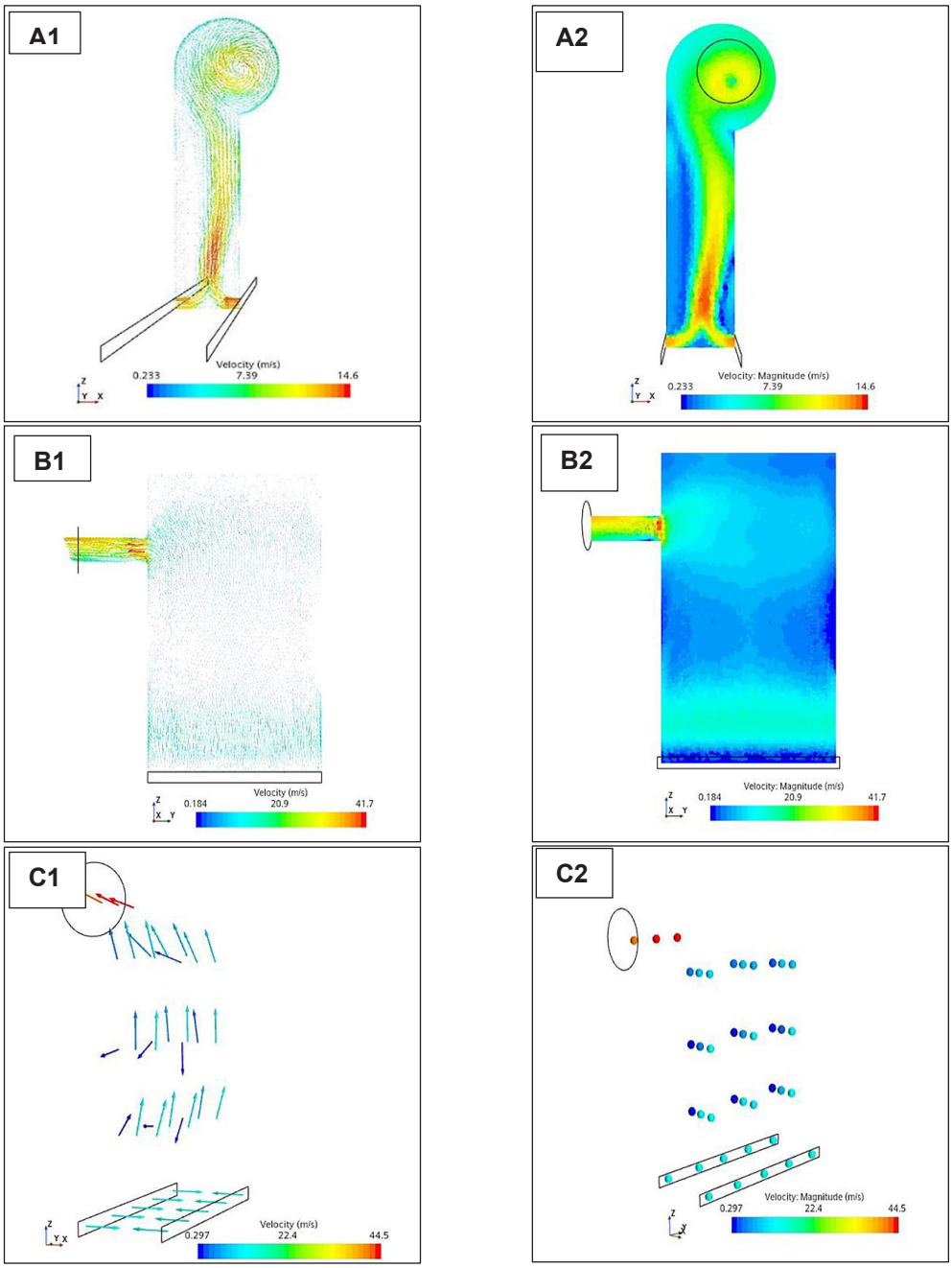

Fig 8: CFD simulation results portraying planar views of velocity vectors (A1, B1 and C1) and velocity scalars (A2, B2 and C2) of the airflow in the suction nozzle for the medium flow system.

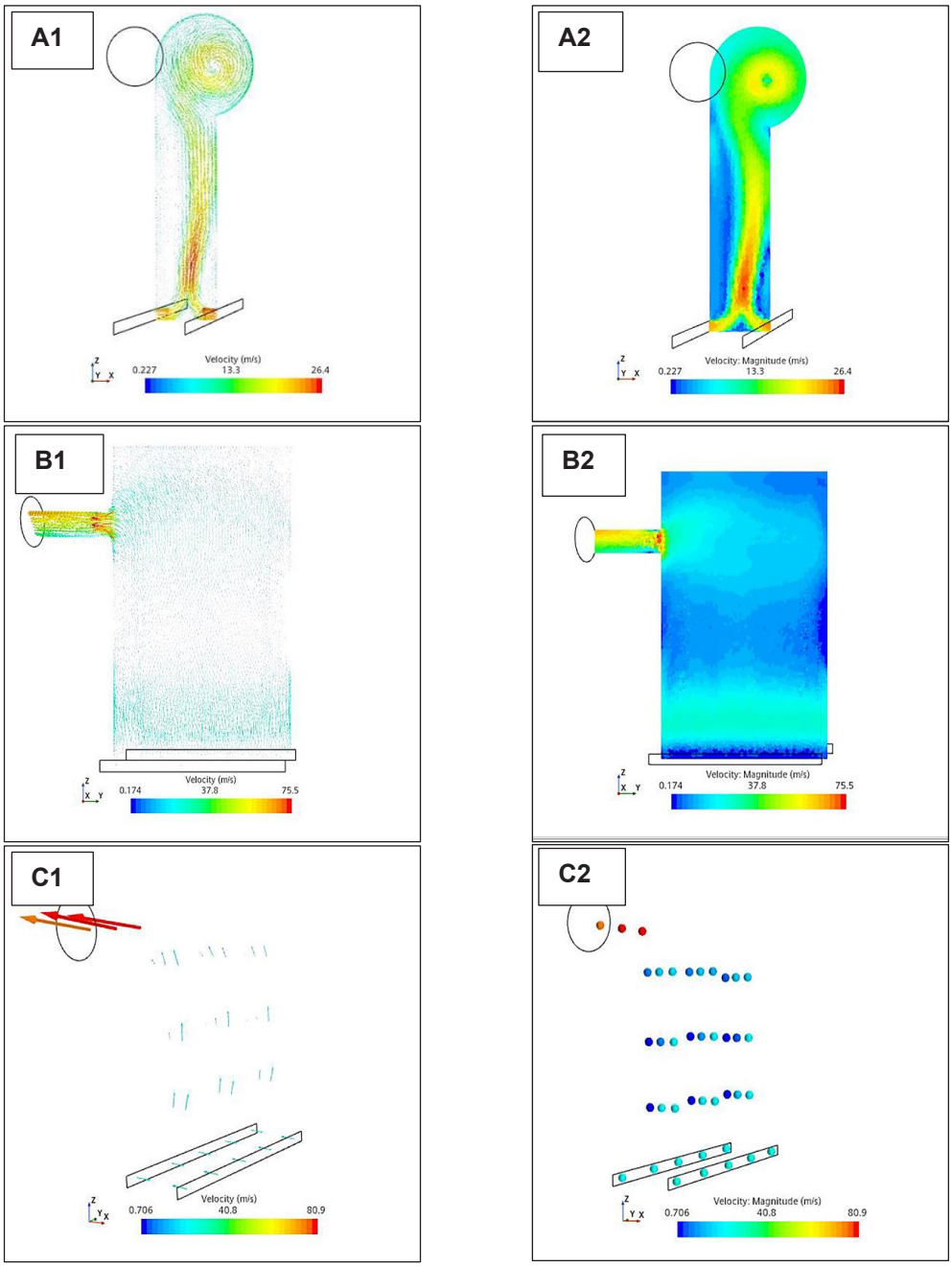

Fig 9: CFD simulation results portraying planar views of velocity vectors (A1, B1 and C1) and velocity scalars (A2, B2 and C2) of the airflow in the suction nozzle for the high flow system.

6 Discussion

Across all three flow intensities (low, medium, and high), the model demonstrates accurate predictions regarding the magnitude and direction of velocities within both inlets and the connecting pipe. This is evidenced by the high R^2 values and the corresponding low RMSE

statistics specific to these sections. However, less precise predictions are observed for the velocities simulated in the fluidizing box. The desired high R^2 values, coupled with the undesired high RMSE values relative to the average velocity in the fluidizing box, indicate that the model's predictions in this region are less accurate. Nonetheless, it is noteworthy that these predictions consistently exhibit a constant bias, as evidenced by the high R^2 values. Despite the suboptimal performance of the predictions in the fluidized box, the predictor strongly influences the observed value. The underlying issue lies in the model's inability to fully capture this influence of the vortex section within the fluidizing box [17].

An important observation is that both the observed and simulated data exhibit consistent trends of higher and lower air speeds developing across the length, width, and height of the fluidizing box. The model, however, consistently tends to overestimate the velocity near the other-side wall, while simultaneously underestimating the velocity at the fan-side wall. In contrast, the experimental velocities demonstrate the highest values in the centre of the fluidizing chamber. Moreover, slightly higher inlet velocities are consistently observed in the modelled flow for the other-side inlet as when compared to the experimental flows obtained.

These observations suggest that the model produces a more pronounced S-shape velocity profile compared to the experimental data. Since the formation of the S-shape flow profile is attributed to the development of a vortex in the vortex chamber and connecting pipe, it appears that the model fails to fully capture the complex interactions between the vortex and the upward flowing air. Simulating the interaction between an upward uniform suction flow and a vortex presents several challenges due to the complex nature of the flow phenomena involved. Some reasons why it is difficult to accurately simulate this interaction include:

- Turbulence modelling: The experimental velocities correspond to Reynolds numbers exceeding 2,800, indicating that the flow is classified as turbulent. Turbulence is a highly intricate phenomenon that poses significant challenges in achieving accurate modelling [18]. Numerous turbulence models have been developed, each with its own set of assumptions and limitations. In this study, two turbulence models, namely the K-Epsilon and Reynolds Stress models, were investigated. A comparison of these models resulted in an R^2 value of 0.99 and an RMSE value of 0.24, indicating excellent agreement. Based on its capability to simulate highly swirling or strongly separated flows, the Reynolds Stress model was selected as the preferred turbulence model [11]. However, it is important to acknowledge that the modelled velocities exhibit regions that fall within the laminar or intermittent flow regimes. These regions may introduce additional complexities, as different mathematical formulas are employed for these conditions and the numerical approach of the solution algorithm in STAR CCM+™ comes into play.

- Grid resolution and numerical stability: Resolving the fine-scale features of the vortex and the flow field is crucial for capturing the detailed interactions [19]. However, simulating these fine-scale features requires a high grid resolution, which can be time consuming and require high speed computing power. Additionally, maintaining numerical stability becomes challenging when dealing with sharp flow discontinuities or high gradients associated with vortex structures [12,20].

- Vortex dynamics: Vortices are dynamic structures that can undergo deformation, merging, or splitting depending on the flow conditions. Capturing the accurate evolution of the vortex structure and its interactions with the surrounding flow is a complex task [21]. Simulating the intricate details of vortex dynamics, such as the formation of secondary vortices, vortex shedding, or vortex breakdown [21], requires robust numerical methods and high-resolution simulations [22].

7 Conclusions and recommendations

In general, the simulated velocities exhibit good agreement with the experimental velocities measured in the suction nozzle, except for notable disparities in the velocity magnitudes observed within the fluidizing chamber. These findings provide a comprehensive understanding of the velocity profile, encompassing air speed and flow direction. Such insights are valuable for comprehending particle movement within the separating unit, facilitating optimal system design, establishing operating parameters, and troubleshooting. However, further research efforts should be dedicated to the following areas:

- Simulation and model: To improve the accuracy of velocity predictions within the fluidizing box, it is advisable to explore turbulence models specifically tailored to capture the interaction between the upward airflow and the vortex. Combining different turbulence models and refining the meshing models in that specific region may also prove beneficial.
- Unit design: The current design of the inlet and vortex chamber contributes to the development of a pronounced snaking airflow profile, resulting in significant dead spots and eddying currents within the fluidizing chamber. This suboptimal velocity profile may not be conducive to effective particle fluidization. To address this, a potential improvement involves slightly tapering the inlet outward at a 45-degree angle, allowing the velocity profile to develop uniformly across the entire width of the fluidizing chamber and mitigating the low-flow regions near the walls. Additionally, incorporating a lip in the suction nozzle section where the vortex interacts with the upward flowing air may help reduce the negative influence of the vortex on the velocity profile within the fluidizing chamber.

By addressing these aspects related to simulation and model refinement, as well as unit design optimization, a more accurate representation of velocity profiles in the fluidizing chamber can be achieved, leading to improved performance and efficiency in particle fluidization processes.

This work received support from Gormash Export, Siberia, and the Centre of Excellence in Carbon-Based Fuels at North-West University, Potchefstroom, South Africa. Additionally, this study is partially supported by the National Research Foundation (NRF) of South Africa through the Coal Research Chair Grants with the following grant numbers: 86880, UID115228, UID85632. The opinions, findings, conclusions, or recommendations expressed in this work are those of the author(s), and the NRF assumes no liability in this regard.

References

1. Zhou, C. et al. Recent progress and potential challenges in coal upgrading via gravity dry separation technologies. Fuel 305, 121430 (2021).
2. Weinstein, R. & Snoby, R. J. Advances in dry jigging improves coal quality. Min Eng 59, 29–34 (2007).
3. Honaker, R. Q. et al. Upgrading Coal Using a Pneumatic Density-Based Separator. International Journal of Coal Preparation and Utilization 28, 51–67 (2008).
4. Moszko, J. C., Iwaszenko, S., Andrej, B. & Janoszek, T. Novel dry sorter for coal processing and coal recovery from mine originating wastes. in XVIII International Coal Preparation Congress (ed. Litvinenko, V.) 1149–1154 (2016). doi:10.1077/978-3-319-40943-6_180.

5. Stepanenko, A. I. «SEPAIR» pneumatic separation complex for dry coal beneficiation. in XVIII International Coal Preparation Congress 1089–1093 Springer International Publishing, (2016). doi:10.1007/978-3-319-40943-6_170.
6. Stańczyk, K. Modelling of Hard Coal Beneficiation Process Utilising Negative Pressure Pneumatic Separator. Energies (Basel) 13, 5174 (2020).
7. Stańczyk, K., Bajerski, A. & Łączny, M. J. Negative-pressure pneumatic separator: a new solution for hard-coal beneficiation. Int J Coal Sci Technol 8, 103–123 (2021).
8. Rhodes, M. J. Introduction to Particle Technology. Wiley. (2008).
9. Fluidization Engineering. Elsevier, (1991). doi:10.1016/C2009-0-24190-0.
10. Siemens. Simcenter STAR CCM+ User guide, tutorials, knowledge base and technical support. Simcenter STAR CCM+ https://community.sw.siemens.com/s/question/0D54O000061xpUOSAY/simcenter-starccm-user-guide-tutorials-knowledge-base-and-tech-support (2023).
11. Fernandez, P. Physics models in STAR CCM+ (Parts I-IV). The answer is 27 https://theansweris27.com/physic-models-in-star-ccm-part-i/ (2019).
12. Ferziger, J. H., Perić, M. & Street, R. L. Computational Methods for Fluid Dynamics. Springer International Publishing, (2020). doi:10.1007/978-3-319-99693-6.
13. Symscape. Steady-State or Unsteady CFD Simulation? https://www.symscape.com/steady-state-or-unsteady-cfd-simulation (2012).
14. Hildebrand, N. J., Venkatachari, B. S., Srivastava, V., & Choudhari, M. M. Recent Progress on RANS-Based Transition Model Verification. NASA Langley Research Center, (2023).
15. Raje, P., Parish, E., Hickey, J.-P., Cinnella, P., & Duraisamy, K. Recent Developments and Research Needs in Turbulence Modeling of Hypersonic Flows. arXiv:2412.13985, (2025).
16. Anderson, J. D. Computational Fluid Dynamics: The Basics with Applications. (2017).
17. Wheeler, W. Evaluating linear regression models using RMSE and R2. Medium https://medium.com/wwblog/evaluating-regression-models-using-rmse-and-r%C2%B2-42f77400efee (2021).
18. Wicox, D. C. Turbulence Modeling for CFD. Dcw Industries, Incorporated, (2006).
19. Oberkampf, W. L. & Roy, C. J. Verification and Validation in Scientific Computing. Cambridge University Press, (2010). doi:10.1017/CBO9780511760396.
20. Tsoutsanis, P. et al. Comparison of structured- and unstructured-grid, compressible and incompressible methods using the vortex pairing problem. Compute Methods Appl Mech Eng 293, 207–231 (2015).
21. Zhou, J., Chen, Y., Li, D., Zhang, Z. & Pan, W. Numerical simulation of aircraft wake vortex evolution and wake encounters based on adaptive mesh method. Engineering Applications of Computational Fluid Mechanics 14, 1445–1457 (2020).
22. Van Jindelt, T., van der Burg, J. W., van der Weide, E. T. & Hoeijmakers, H. W. Numerical Investigation of Vortex Breakdown. in 34th AIAA Applied Aerodynamics Conference. American Institute of Aeronautics and Astronautics, (2016). doi:10.2514/6.2016-4174.
23. Mimeau, C. & Mortazavi, I. A Review of Vortex Methods and Their Applications: From Creation to Recent Advances. Fluids 6, 68 (2021).